

Densely-packed particle raft at vertically vibrated air-water interface

Xiuhe Yan,^{1,*} Tabitha C. Watson,^{1,*} and Hongyi Xiao^{1,†}

¹*Department of Mechanical Engineering, University of Michigan, Ann Arbor, USA*

(Dated: February 20, 2026)

We investigate the dynamics of a dense raft of millimeter-sized granular particles at a vertically vibrated air-water interface, which displays a rich set of patterns and particle dynamics as we vary the vibration amplitude, frequency, and particle packing fraction. While the classical parametric instability with standing waves still occurs over a certain parameter space, the measured wave dispersion relations indicate an increasing role in the raft's emerging elasticity at higher packing fractions, which induces a decrease in the effective surface tension and an increase in an out-of-plane bending modulus. At higher vibration frequencies and lower amplitudes, we also identified a regime without standing waves in which individual particles exhibit thermal-like motion and transition from diffusive to sub-diffusive transport as the packing fraction increases. Glassy behaviors such as spatial and temporal heterogeneity in particle dynamics occur as well, which is analogous to supercooled liquids. When the vibration amplitude is increased starting in this supercooled regime, a large cavity eventually forms inside the raft with its size and shape related to the vibration frequency and the injected vibration energy. The cavitation results in the coexistence of free surface water waves inside the cavity and thermal-like particle motion in the raft.

I. INTRODUCTION

Particles residing at an interface between two fluids can assemble into a raft via attractive capillary interactions [1], which arise from the energy minimization of the distorted liquid interface [2–4]. Particle rafts have wide applications such as in self-assembly, interfacial stabilization, and pollution control [1]. As particles are macroscopic and observable, rafts are also ideal model systems for understanding the packing structure and dynamics of out-of-equilibrium systems, such as athermal amorphous solids [5, 6]. They also share similarities with living matter at interfaces, such as fish bubble nests [7] and rafts of mosquito eggs, fire ants, and starfish embryos [8, 9], which may exhibit more dynamic behaviors due to their internal activity or environmental fluctuations. However, due to the complex and many-body nature of the capillary and hydrodynamic interactions [10, 11], the dynamics and pattern formation of particle rafts are far from being well-understood.

Particles at a fluid interface often pack densely and exhibit solid-like features collectively [1]. Several studies have examined the mechanical failure of particle rafts via imposing tensile strains [5, 6, 12, 13] and introducing surfactants [14, 15]. In these tests, the rafts often demonstrate a certain degree of elasticity before failure via solid-like fracturing [14, 15] or shear band formation [5]. Other studies have explored the transition between ductile fluid flow and brittle granular behavior in granular rafts under quasistatic rotary shear where shear bands and nonlocal effects appear [16]. Moreover, the deformation of particle rafts can be complicated by out-of-plane motion induced by compression and indentation [14, 17–20], which

can result in the raft buckling and collapsing [21–24]. In this case, a bending modulus emerges to resist the change in the surface energy due to the induced curvature of the interface, as the liquid-particle contact angle needs to be maintained [25–27]. While many solid-like aspects like these have been discussed for particle rafts, their liquid-like features are less understood because particle rearrangements are hindered by attractive interactions (except for similarly-charged colloids) and strong dissipation from friction and viscosity. This calls for experiments with more dynamic excitations.

Under dynamic excitation, hydrodynamic particle interaction and underlying fluid flow can become important in addition to capillarity [28–31]. While several studies have examined dynamical excitations of floating particles at low densities [32–35], less is known about densely-packed particle rafts which may introduce viscoelasticity to the liquid interface. Generating surface waves using vibration can be an effective method to induce dynamic excitations, and based on this, important raft properties such as the bending modulus can be probed from the observed wave dispersion [28]. Propagating surface waves can trigger the fragmentation of a raft, resulting in a floe-size distribution similar to that of floating sea ice [29]. This is related to viscous stresses from the underlying fluid, a mechanism that is absent in quasi-static processes. However, in studies that have examined this, the waves were induced from a vibrating source placed directly at the free surface, e.g., a vertically vibrating intruder, making the raft dynamics intrinsically heterogeneous. To impose homogeneous and dynamic excitation, it is possible to vertically shake the entire liquid container to trigger surface waves formed due to hydrodynamic instability, e.g., Faraday waves [36]. Still, the corresponding collective particle dynamics and emergent pattern formation remain largely unexplored.

Under periodic vertical oscillations, a liquid interface can exhibit Faraday waves when the vibration ampli-

* These two authors contributed equally to the work.

† hongyix@umich.edu

tude exceeds a critical threshold. This comes from the parametric Faraday instability in which standing waves emerge and oscillate typically at half the driving frequency. The wave formation depends on several parameters, including the excitation frequency, vibration amplitude, and the fluid’s physical properties including density, viscosity, and surface tension [37–39]. Higher excitation frequencies generally lead to shorter wavelengths and higher threshold accelerations, whereas increasing the fluid viscosity or surface tension tends to stabilize the surface against wave formation. By varying these control parameters, various spatial patterns can be obtained, such as stripes, squares, and hexagons, which represent different modes of parametric resonance [36, 40–42].

Interestingly, the original manuscript by Faraday in 1831 [36] was attached to another manuscript discussing patterns formed by a layer of particles on a vibrating plate, which also shows rich phenomena arising from energy transfer via inelastic particle collisions [30, 43–49], such as the formation of subharmonic standing waves [43] and energy localization [44]. Here, we combine both systems and consider a dense raft of granular particles on a vertically vibrated air-water interface. While the dynamics of Faraday waves on a liquid surface can be described by the incompressible Navier–Stokes equations with associated kinematic boundary conditions [40, 50, 51], the addition of a dense layer of particles can induce additional dissipation and elasticity to the interface. This setup then leads to two coupled questions of how densely-packed particles influence the wave patterns, and how vertical vibration excites particle dynamics, which can be intriguing when the supposed wavelength approaches the particle size.

In this study, we experimentally investigate the pattern formation and particle dynamics of dense granular rafts at a vertically vibrated air-water interface. By systematically varying the particle packing fraction, vibration frequency, and amplitude, we identified distinct regimes in raft behaviors including not only the formation of standing waves, but also a glassy regime in which waves disappear and particles exhibit thermal-like dynamics as well as a regime in which a large cavity in the raft develops. We then performed quantitative measurements, including the wave dispersion relation, to understand how particle dynamics and particle-fluid interaction influence these observed phenomena. Besides implications on relevant real-world systems, the rich physics revealed in our experiments demonstrates that particle rafts can serve as model systems for understanding the implications of complex particle interactions to a variety of problems beyond the elastoplastic behavior of solids.

II. EXPERIMENTAL METHODS

We constructed an experimental apparatus to vertically vibrate a dense granular raft, see the schematic in Fig. 1. The container has a square cross-section with

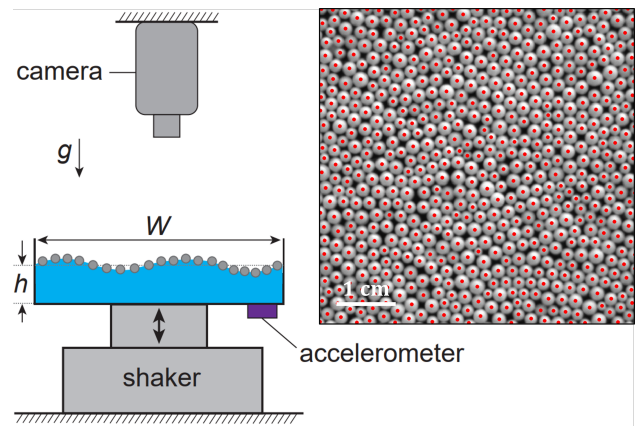


FIG. 1: Schematic of the experiment with a vibrated particle raft and an example snapshot with tracked particle centers labeled as red dots.

$W = 10.9$ cm and is filled with deionized water with a depth of $h = 5$ mm. The container, driven by a shaker, experiences a sinusoidal oscillation of its vertical position, $Z(t) = A \sin(2\pi ft)$, with frequency f and amplitude A . We used an accelerometer to monitor the container’s acceleration amplitude a , and calculated the displacement amplitude via $a = 4\pi^2 f^2 A$. We tested various frequencies in a range $f \in [20, 100]$ Hz and amplitudes in a range $A \in [0.02, 0.2]$ mm.

The particles are closed-celled Styrofoam spheres with a density of $\rho_p \approx 15$ kg/m³, which is small compared to the nominal density of water, $\rho = 1000$ kg/m³. Two batches of size polydisperse particles were tested with different mean diameters, $d = 1.4 \pm 0.2$ mm and $d = 2.1 \pm 0.2$ mm, respectively. While the small particles are useful for studying pattern formation, the large particles present an easier case for tracking and studying individual particle dynamics. Prior to each experiment, we deposited particles on the water surface and removed stacking particles to obtain a strict monolayer. We define the particle packing fraction ϕ as the ratio between the projected area occupied by the particles divided by the cross-sectional area of the container.

For observing pattern formation, images with a resolution of 2448×2048 px² were recorded by a camera at 73 Hz. Particle positions were extracted using a standard circular Hough transform phase-coding method (available in MATLAB) to detect centers for the circular projections of the particles [52], with an example result shown in Fig. 1. To estimate the area fraction ϕ , we binarized an image of the initial packing configuration without vibration and calculated ϕ based on the number of pixels belonging to the particles. Varying the binarization threshold within the reasonable range may influence the obtained packing fraction systematically up to 2.4%. To obtain the intra-cycle particle dynamics, we used a high-speed camera to monitor a few selected cases, which captures images at 460 Hz with a resolution of 2448×1024 px².

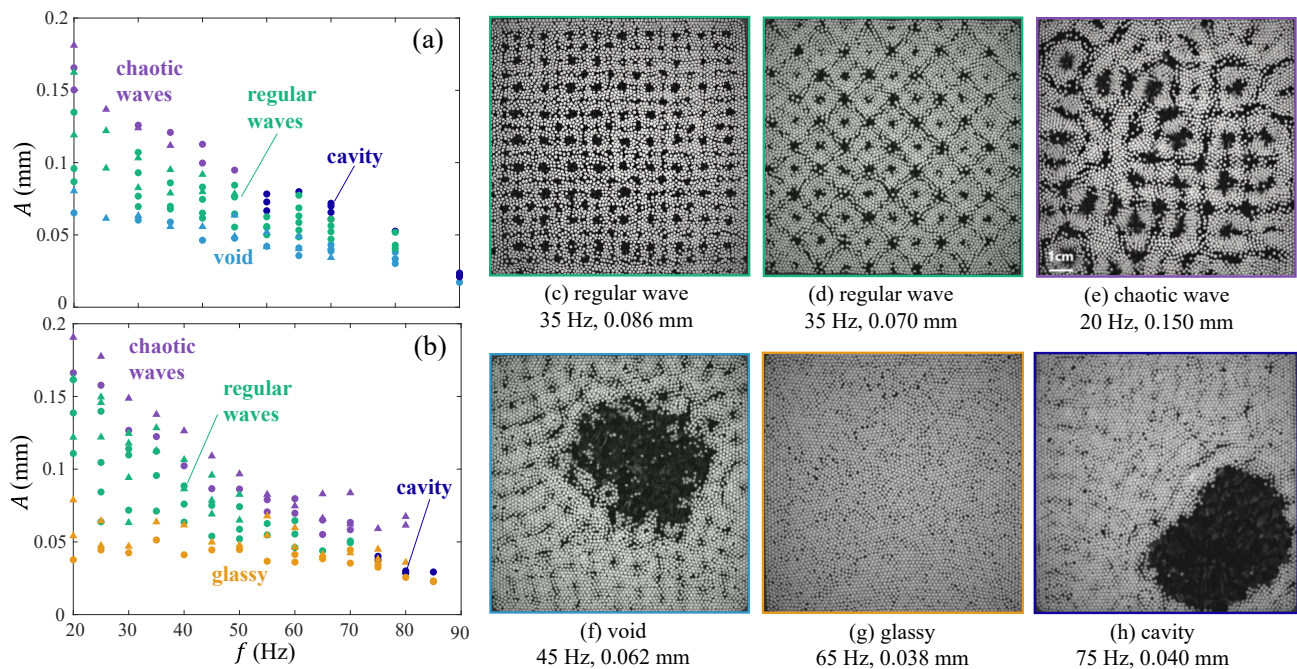


FIG. 2: Phase diagram at packing fractions (a) $\phi = 0.77$ and (b) $\phi = 0.90$. The circles represent the data for particles with $d = 1.4$ mm, and the triangles for $d = 2.1$ mm. (c)-(h) Experimental snapshots for the respective regimes. Specifically, (e)(f)(h) are from $\phi = 0.77$ and (c)(d)(g) are from $\phi = 0.90$.

III. PATTERN FORMATION IN VIBRATED RAFTS

Under different vibration amplitudes A , driving frequencies f , and particle packing fractions ϕ , a raft exhibits distinct dynamics and patterns, which are summarized in Fig. 2a and b for $\phi = 0.77$ and $\phi = 0.90$, respectively. Both results for $d = 1.4$ mm and $d = 2.1$ mm are shown, although their general behaviors are similar, which we categorize to the following five types.

We first identify a regime having regular patterns formed by standing waves, such as the square-shaped and x-shaped patterns shown in Fig. 2c and d, which closely resemble the Faraday instabilities of a pure liquid system. Particles near the wave antinodes pack loosely, making the periodicity obvious. Other patterns also exist in this regime, such as striped patterns which have only one family of waves along a single direction. In Fig. 3, we show side views of the raft over two vibration cycles, with time normalized by $T = 1/f$. At $t/T = 0.5$ and $t/T = 1.5$ no peaks are observable, corresponding to the time instances in which the interface is flat. At both $t/T = 0$ and $t/T = 1$, two sets of wave peaks are observed, but occur at different locations offset by half the wavelength, which indicates that the standing waves have a period of $2T$. Hence, they oscillate at half the driving frequency like the classical Faraday waves due to parametric resonance [40, 50, 51]. These results suggest that, in this regime, the presence of particles do not fundamentally alter the classical physics of the Faraday instability. The

influence of the particles will be discussed in Sec. IV.

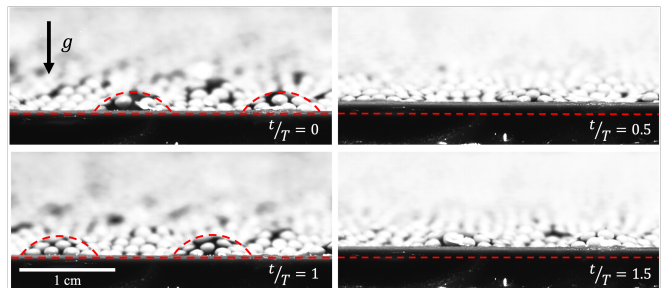


FIG. 3: Time series of vibrated raft of $d = 1.4$ mm particles in standing-wave regime, $A = 0.086$ mm, $f = 35$ Hz, demonstrating that wave frequency is half of the vibration frequency.

At small to intermediate frequencies, a transition to a chaotic regime occurs for both $\phi = 0.77$ and $\phi = 0.90$ as we increase the amplitude A . The wave patterns are no longer regular and stable, see an example in Fig. 2e. The transition amplitude is lower with increasing frequency, indicating a relation to the injected vibration energy, proportional to $A^2 f^2$. This regime is also present in a pure liquid system [43, 53, 54], although it is likely that strong fluctuations in the local particle packing structure may facilitate the transition.

The following three regimes to be discussed have no counterpart phenomena in a pure liquid system. If we decrease the amplitude from that of the regular pattern-forming regime, the particles are less agitated and pack

closely with their neighbors. For the lower packing fraction that was tested, $\phi = 0.77$, there are not enough particles to fully cover the entire area, which leads to a void forming in the raft that co-exists with standing waves, see Fig. 2f.

For the higher packing fraction, $\phi = 0.90$, the raft behavior is qualitatively different at lower amplitude, $A \approx 0.5$ mm, and exhibits neither standing waves nor a void. Instead, a relatively uniform yet disordered packing structure is observed and individual particles vibrate with a thermal-like motion, see example in Fig. 2g. As discussed later in Sec. V, particles may be confined by their neighbors and show a sub-diffusive and glassy behavior.

At higher frequencies, $f \approx 70$ Hz, a more peculiar regime emerges, characterized by a cavity forming in the raft, creating a highly dense layer of particles around it with the rest of the raft exhibiting glassy behavior, see Fig. 2g. Here, we use the term cavity to distinguish from the void formed at the lower density due to having insufficient number of particles to cover the liquid surface. However, for $\phi = 0.77$, similar phenomena is also observed at amplitude above the regular pattern regime, see Fig. 2a, so it might be reasonable to merge this regime with the void-forming regime due to the similarities.

Lastly, we note that results with both high frequency and high amplitude are not included, as water or particles may be ejected due to the high energy input, making the experiments unsustainable. As the observed raft behaviors are rich, understanding the role of particles in the formation, stability, and transition for all the observed regimes is a sophisticated task that goes beyond this work, especially for the transient behavior in the chaotic regime. We will focus on characterizing the steady-state behaviors of the regular wave regime, the glassy regime, and the cavity-forming regime.

IV. DISPERSION RELATIONS IN REGULAR WAVE PATTERNS

In the regular wave regime, we investigate how the presence of particles influences the dispersion relation, which links the wave's oscillation frequency and spatial periodicity. For inviscid and incompressible fluids, a classical dispersion relation is

$$\omega^2 = \left(gk + \frac{\gamma}{\rho} k^3 \right) \tanh(kh), \quad (1)$$

where ω is the angular frequency of the surface wave, k is the wavenumber, g is the gravitational acceleration, and γ is the surface tension, which is 72 mN/m for water. The term $\tanh(kh)$ accounts for a finite fluid depth. The terms gk and $(\gamma/\rho)k^3$ represent the gravitational and capillary restoring forces, which dominate at long and short wavelengths, respectively. Setting these two terms equal yields the capillary length, $1/k = \sqrt{\gamma/g\rho}$, which is about 2.7 mm for water, corresponding to $k \approx 370$ and

the wavelength $\lambda = 2\pi/k \approx 1.7$ cm. This is on the same order of magnitude as the wavelengths in Figs. 2 and 3, indicating that both effects are at play.

For a particle raft, having densely-packed particles may alter both the effective surface tension and the inertia of the interface. At high packing fractions, the particles may repel each other when they are in contact, resulting in a reduced surface tension, γ_e , which is referred to as the effective stretching modulus [28]. Moreover, as standing waves distort the curvature of the liquid surface between particles, a bending modulus, B , emerges as the raft resists out-of-plane deformation. The dispersion relation can then be modified as,

$$\omega^2 \left(1 + \frac{\rho_r}{\rho} a_p k \right) = gk \left(1 + \frac{\gamma_e k^2}{\rho g} + \frac{Bk^4}{\rho g} \right) \tanh(kh), \quad (2)$$

where the k^5 term accounts for out-of-plane bending by treating the raft as a thin elastic sheet [55]. An additional factor on the left-hand side is included to consider the added particle inertia, in which $\rho_r = \rho_p \phi$ and $a_p = 2d/3$ are the effective density and thickness of the raft [28], respectively. As $\rho_p \ll \rho$ for Styrofoam particles, the added inertia is small. This formulation was introduced to model waves in a particle raft induced by a vibrating plate at the interface [28], which may also be applicable to our experiments.

Here, we focused on the square-shaped wave patterns and tested five different packing fractions ϕ for the smaller particles with $d = 1.4$ mm. At each ϕ , we extracted a dispersion relation by testing various vibration amplitudes and frequencies. In each experiment, we performed a time-average for all frames and obtained a single image to capture the periodicity, see Fig. 4a. A two-dimensional Fourier transform was then applied to the image to determine the dominant wave number k , as demonstrated in Fig. 4b. As shown earlier in Fig. 3, the corresponding angular frequency is $\omega = \pi f$.

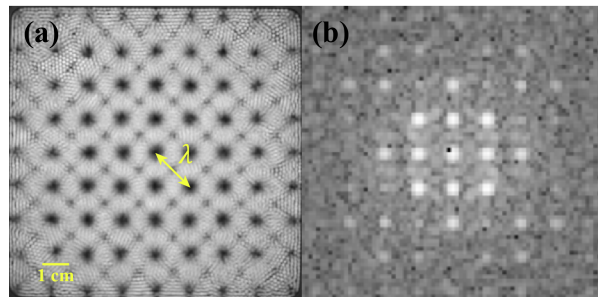


FIG. 4: (a) A time-averaged experimental image in the regular wave regime for $d = 1.4$ mm, $f = 20$ Hz, $A = 0.124$ mm, and $\phi = 0.8113$. (b) The corresponding two-dimensional Fourier transform result, indicating a wavelength of $\lambda = 1.72$ cm.

Our measured dispersion relations indicate that k increases with ω with a slightly non-linear trend, see two examples at different packing fractions in Fig. 5a and

b. For $\phi = 0.77$, both Eqs. 1 and 2 can be well-fitted to the measurements, with the coefficients of determination, $R^2 > 0.95$. However, for a higher packing fraction, $\phi = 0.90$, the modified relation, Eq. 2, better captures the non-linearity in the dispersion relation, indicating a stronger presence of the bending rigidity via the Bk^5 term.

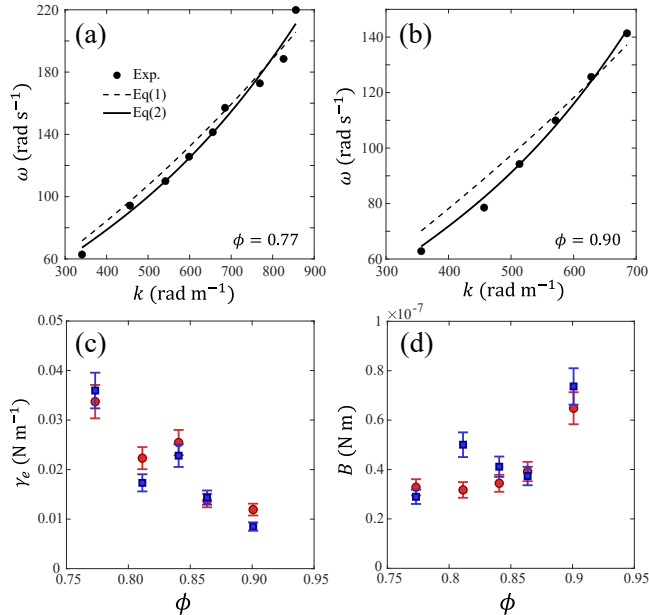


FIG. 5: Regular standing wave patterns for $d = 1.4$ mm. (a) Experimental result of angular frequency vs. wave number (circles) for $\phi = 0.77$. The dashed curve represents the fitted Eq. 1, with $R^2 = 0.97$, and the solid curve is fit to Eq. 2, with $R^2 = 0.98$. (b) Experimental result (circle) for $\phi = 0.90$, Eq. 1 (dashed curve) with $R^2 = 0.95$, and Eq. 2, with $R^2 = 0.99$. (c) and (d) are the fitted stretch modulus γ_e and bending modulus B fitted at various packing fractions ϕ , receptively. Red circles are results from linear fitting and blue squares are from non-linear fitting to Eq. 2. Error bars represent one standard deviation of the uncertainty estimated from fitting residuals.

We next examine the fitted stretching and bending moduli as a function of the packing fraction, see Fig. 5c and d. To test the sensitivity of the results to the fitting method for Eq. 2, we used both direct non-linear least squares fitting between w and k and an alternative linear fitting, in which we treat the entire left-hand side as the dependent variable and the three non-linear terms on the right-hand side as independent variables, e.g., $\tanh(kh)Bk^5/\rho$. In our case, the factor $\tanh(kh) \approx 1$, while the added inertial term $\rho_r ak/\rho \ll 1$, so they are not influential to the result. The two fitting methods yield similar values of γ_e and B , with an anomaly for B at $\phi \approx 0.81$, which is likely due to experimental noise.

The effective surface tension γ exhibits a consistent monotonic decrease for higher packing fraction ϕ , see Fig. 5c. This is likely due to the particles replacing and distorting the free liquid-air interface, while devel-

oping repulsive steric contact at higher ϕ . The bending modulus B increases slowly with ϕ at low-to-moderate ϕ but rises rapidly towards the highest tested value at $\phi = 0.90$, see Fig. 5d. The rapid increase occurs possibly due to the fact that as ϕ increases, particles become significantly caged by their neighbors and a persistent contact force network develops, including both elastic and frictional particle contact forces, which may give rise to additional bending rigidity. The measured dependence of γ_e and B on ϕ qualitatively agrees with prior experimental measurements in rafts under other forms of excitations [18, 28, 56]. However, given that the specific particle packing structure in our system is organized by the standing waves, it is likely that the structure-property relation is unique for the emerging elastic-like behavior of the vertically vibrated raft.

V. GLASSY PARTICLE DYNAMICS IN DENSE PACKINGS

In the regime with glassy particle dynamics, no visible standing waves exist and individual particles vibrate in cages formed by their neighbors in short times, while rearranging their packing structure in longer times, resembling the dynamics of particles in a supercooled liquid [57]. To conduct quantitative analysis, we used the larger particles with $d = 2.1$ mm to conduct a series of experiments at various packing fractions, $\phi \in [0.88, 0.91]$, using a relatively high frequency $f = 65$ Hz and low amplitude $A = 0.05$ mm, with respect to the parameter space covered in the phase diagram in Fig. 2b. The larger particles were chosen for the higher-frequency tests to approximate the limit when the supposed wavelength $\lambda \approx d$, which may suppress wave formation and wave-induced correlated particle motion. To obtain particle trajectories over time, we zoomed into a sub-region of the raft and captured images with a resolution of 864×860 px² and a frame rate of 186 Hz.

For each packing fraction, we first calculated the particles mean-squared displacement (MSD) over time,

$$\text{MSD}(\tau) = \langle |\mathbf{r}(t + \tau) - \mathbf{r}(t)|^2 \rangle_t,$$

where $\mathbf{r}(t)$ is the position of a particle at a starting time t and τ is the lag time over which the displacement is considered. In glassy behaviors, particles are sub-diffusive at intermediate τ , reflecting the confinement of particles within cages. The relation between the MSD and τ can then be characterized as

$$\text{MSD} \sim \tau^\alpha,$$

with the exponent $\alpha \approx 0$ indicating a glass state, while $\alpha \approx 1$ indicates normal diffusion.

In the most dilute case considered, $\phi = 0.886$, the particles have normal diffusive motion, which is made clear with the reference line of $\alpha = 1$ in the MSD plot in Fig. 6. In the densest case considered, $\phi = 0.907$, the behavior of

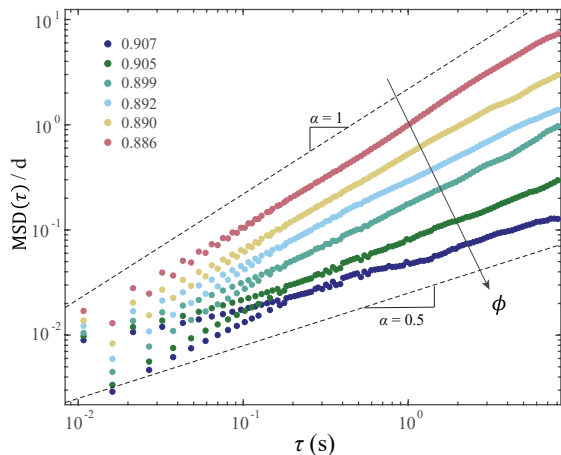


FIG. 6: The mean squared displacement of $d = 2.1$ mm particles normalized by particle diameter with various packing fractions at $f = 65$ Hz and $A = 0.052$ mm.

the raft is clearly sub-diffusive, as $\alpha \approx 0.5$, implying that the motion of individual particles is highly constricted by their neighbors within our duration of observation. Thus, over a tight range of ϕ , the vibrated raft exhibits qualitatively different behaviors, with the slow down in its dynamics resembling that of a thermal particle system evolving towards the glass transition as it is compressed or cooled.

Beyond averaged particle motion, we further consider the probability distribution of individual particle displacements, $\{\Delta r_x, \Delta r_y\}$, over a given lag time. We subtracted the mean from each distribution to account for the rigid body translation in the sub-region we monitored. Fig. 7 shows the displacement probability distributions for three example packing fractions measured for a lag time of $\tau = 0.33$ s, which can be well fitted to Gaussian distributions. This indicates a resemblance with particle motion in a thermodynamic equilibrium, even though our particles are driven by external vibration. This is likely a result of the diminishing wavelength of the standing waves and frequent particle collisions in this dense regime, leading to each particle experiencing rather random driving forces.

Visualizations of individual particle trajectories over three seconds are shown in Fig. 8 for the three example packing fractions. For the highest packing fraction, Fig. 8a, the particles mainly oscillate back and forth and rarely leave their effective cages. For the lowest packing fraction, all particles exhibit diffusive trajectories and have higher mobility within the same time period, as seen in Fig. 8d. At the intermediate packing fraction, Fig. 8c, while there is an observable effect from caging on particle trajectories, mobility is increased and some particles have non-trivial displacements with correlation to that of their neighbors. This correlated motion is also present at the highest packing fraction, shown in Fig. 8b, which shows a separate region of the system at the same time shown in Fig. 8a, suggesting that the dynamics are spa-

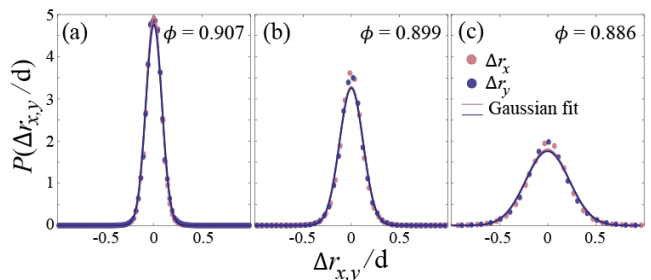


FIG. 7: Displacement probability distributions of the two components of displacement over $\tau = 0.33$ s for $d = 2.1$ mm particles in a raft measured for $A = 0.052$ mm and $f = 65$ Hz at (a) $\phi = 0.907$, (b) $\phi = 0.899$, and (c) $\phi = 0.886$. Bin sizes of (a) 0.025, (b) 0.05, and (c) 0.1 were used. A fitted Gaussian distribution is shown for each displacement component at each packing fraction.

tially heterogeneous.

Dynamical heterogeneity is a hallmark of supercooled liquids close to the glass transition [58] and confined granular particles under slow shear near the onset of jamming [59, 60], both of which are relevant to our current system. As such a system experiences denser packing or lower temperature, its dynamics slow down and become more heterogeneous while simultaneously showing rapid growth of length- and time-scales in the correlations of particle motion. This can be quantified by the four-point susceptibility, χ_4 , which assesses the correlation between the dynamics at any two spatial locations over a given time interval [61]. The calculation is based on measuring the overlap between two configurations. For a system with N particles, we first calculate the self-overlap order parameter over a delay time τ ,

$$q_s(\tau) = \frac{1}{N} \sum_{i=1}^N w(|\mathbf{r}_i(\tau) - \mathbf{r}_i(0)|),$$

where \mathbf{r}_i is particle position and w is chosen to be a step function [61] such that $w = 1$ if the particle displacement $|\mathbf{r}_i(\tau) - \mathbf{r}_i(0)| < 0.3d$ and $w = 0$ otherwise. The susceptibility can then be calculated as

$$\chi_4(\tau) = N \left(\langle q_s^2 \rangle - \langle q_s \rangle^2 \right),$$

in which $\langle \cdot \rangle$ denotes averaging over all starting times, as was true for the MSD calculation. Under this definition, a large χ_4 indicates stronger dynamical heterogeneity.

The measured relation between χ_4 and the delay time τ for a given packing fraction is similar to that of a glassy system, as shown in Fig. 9a. At small τ , all particles vibrate within their respective cages, resulting in $\chi_4 \approx 0$, while at large τ , all particles have diffused, also resulting in $\chi_4 \approx 0$. At intermediate τ , χ_4 reaches a peak value at time τ^* , setting a timescale for when dynamical heterogeneity is strongest. As the packing fraction increases, τ^* increases exponentially with ϕ , see Fig. 9b, indicating

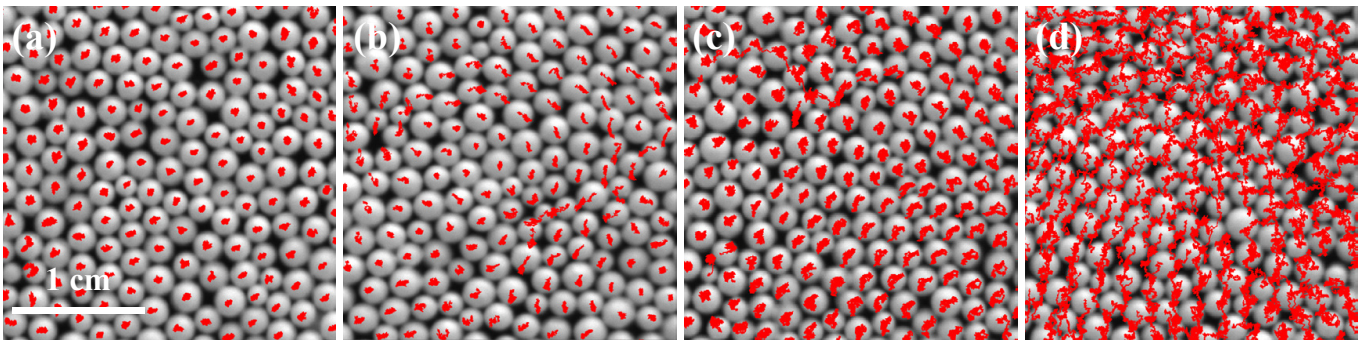


FIG. 8: Particle trajectories for $d = 2.1$ mm particles over $\tau = 3$ s, measured for $A = 0.052$ mm and $f = 65$ Hz in (a) and (b) $\phi = 0.907$, (c) $\phi = 0.899$, and (d) $\phi = 0.886$. While certain regions in the $\phi = 0.907$ case exhibit lower mobility, particles oscillating within effective cages imposed by surrounding regions as shown in (a), other regions in the same system over the same observation exhibit collective rearrangement, as shown in (b). Particle trajectories demonstrate increased mobility in the intermediate density with correlated motion being exhibited by some particles, as shown in (c). These spatially heterogeneous dynamics are distinguished from the diffusive behavior seen in the more dilute case in (d).

rapid slow down in the dynamics to develop correlated motion.

While the growth of τ^* fits the classical description of dynamical heterogeneity for glassy systems, the peak value of χ_4 increases non-monotonically with ϕ , as seen in Fig. 9a, which may reflect two unique features in our vibrated raft. First, as ϕ increases, the standing waves

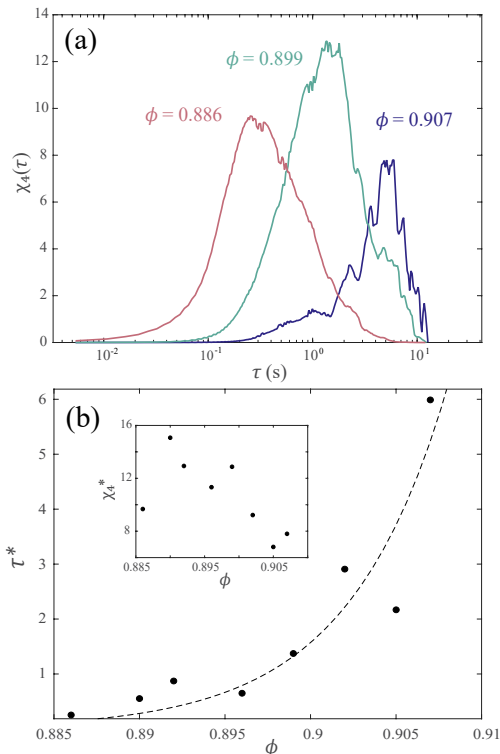


FIG. 9: (a) The four-point susceptibility χ_4 vs. delay time τ measured for three example packing fractions. (b) Dependence of the dynamical timescale τ^* on the packing fraction ϕ . The inset in (b) shows the behavior of the peak value χ_4^* with increasing ϕ .

further diminish due to the more frequent particle collisions and the increased out-of-plane bending rigidity as in Fig 5d. The disappearance of the waves de-correlate the motion of nearby particles and thus decrease the dynamical heterogeneity. Second, at the vertically vibrated interface, a highly-confined particle has the option to move slightly out-of-plane, which may discourage the formation of strong contact force networks and thus de-correlates the motion of nearby particles. This makes the effective interaction potential between particles softer and the raft weakly compressible. These two mechanisms may compete with the traditional role of density in the dynamical heterogeneity.

VI. CAVITY FORMATION IN PARTICLE RAFTS UNDER HIGH-FREQUENCY AND HIGH-AMPLITUDE VIBRATIONS

Starting from the glassy regime in the frequency range $f \in [75, 95]$ Hz, we can reach the cavity-forming regime by increasing the vibration amplitude until a critical value A^* , at which a cavity appears. Upon nucleation, a cavity rapidly expands within a few seconds, before reaching a steady size and shape. The size of a cavity is represented by a diameter L of an equivalent circle with the same area, which is at least one order of magnitude larger than the particle diameter, see a high-speed image in Fig. 10a. Free surface waves are observed inside the cavity, suggesting lesser damping there due to the lack of particles. Increasing the amplitude beyond A^* will result in the cavity expanding further, and water droplets may sputter, as seen in Fig. 10b. Here, we focus on understanding the critical condition at which the cavity first appears.

In traditional acoustic cavitation, a cavity nucleates, expands, and rapidly collapses due to pressure fluctuations in a liquid. In our system, however, the cavity is stable, suggesting that the closing pressure from the

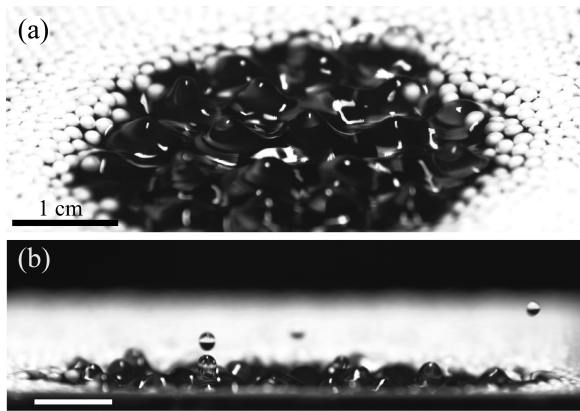


FIG. 10: Snapshots of the cavity and its immediate neighborhood, viewed from (a) an inclined perspective and (b) a side perspective.

surrounding dense raft is balanced by a mechanism that drives particles outward. This is likely related to the interaction between particles and the free surface waves of the water inside the cavity, as shown in Fig. 10a. In our experiments, particles tend to migrate away from liquid surfaces that experience intense vertical oscillations, i.e., the antinodes of the surface waves. Due to this effect, a particle in the cavity may hop between the nodes of the free surface waves and eventually end up in the surrounding raft, which does not have standing waves and pins the nodes of the nearby free surface waves. While individual particles occasionally re-enter the cavity, as seen in the upper right region of Fig. 10a, they quickly drift back to the surrounding dense region. Thus, the cavity's size is stable due to the balance between this drifting effect and closing pressure of the surrounding raft.

Following this argument, an important difference can be noticed between the cavitation regime and the regular wave regime that occurs at lower frequencies. While we also see that particles move away from the antinodes of the standing waves in Figs. 3 and 2c-e, the wavelength is so large that particles never evacuate a full wavelength to allow a cavity with free surface waves to develop. As the cavitation regime occurs at higher frequencies where the supposed wavelength is smaller (with or without particles), the physics may be different. To understand the frequency dependence of the cavitation, we performed experiments using the smaller particles with $d = 1.4$ mm at various frequencies f . For each f , we gradually increased the vibration amplitude from the lower end until reaching the critical amplitude A^* , and the result in Fig. 11b shows a lower A^* for higher f .

Given this, we speculate that the role of the amplitude in cavitation should be to induce large local density fluctuations so that a cavity with free surface waves can nucleate. For $A < A^*$, the fluctuating sizes of small voids in the dense packing are still smaller than the wavelength of a free surface wave, and they do not expand. When $A = A^*$, it is then possible that the size of a fluctuat-

ing void exceeds the wavelength of the capillary wave, allowing the void to grow into a cavity that contains free surface waves. As the wavelength is shorter for higher frequency, the required amplitude is smaller, hence the observation in Fig. 2b.

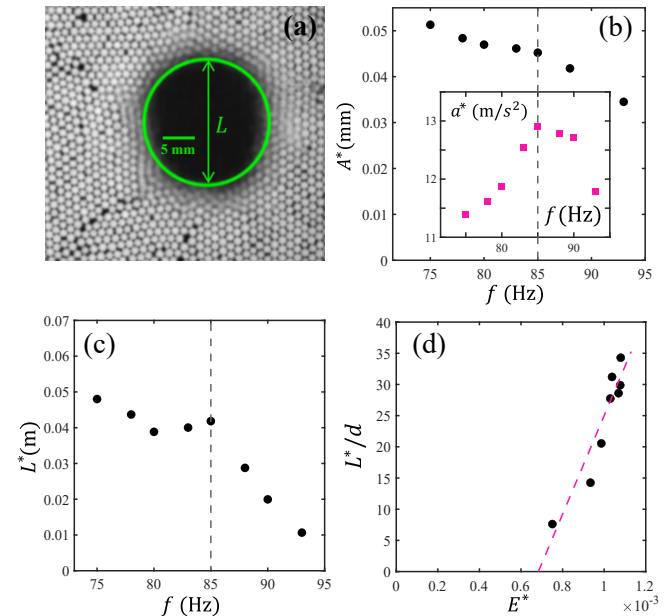


FIG. 11: Cavity formation for the $d = 1.4$ mm particles at packing fraction $\phi = 0.9$. (a) A time-averaged experimental image for $d = 1.4$ mm, $\phi = 0.9008$, $f = 90$ Hz, and $A = 0.029$ mm, with the cavity identified. (b) Critical amplitude vs. frequency. The inset shows the critical acceleration vs. frequency (c) Critical cavity size vs. frequency. (d) Critical cavity size vs. the injected vibrational energy. The black circles are experimental measurements and the dashed line is a linear fit $L^*/d = 7.9 \times 10^4 E^* - 54.1$.

Considering the stabilized size of the void L^* at the critical amplitude, we find that it generally decreases with the vibration frequency, as shown in Figure 11c. This is because the overall energy injected by the shaker decreases for higher frequencies at the critical amplitudes. As the kinetic energy of the container is proportional to $A^2 f^2$, we examine the relation between L^*/d and a characteristic critical energy, $E^* = A^{*2} f^2 / g d$. The result in Fig. 11d shows an approximately linear trend between L^* and E^* , with a cut-off value around $E^* = 7 \times 10^{-4}$, which may correspond to a high frequency at which surface waves always exist in the small voids in a disordered particle packing. Increasing the frequency beyond our range of interest will result in the formation of multiple cavities that are less well-defined and have smaller areas approximately equal to that of a few particles, while still containing surface waves or small ripples.

Lastly, we point out that a small increasing trend in the critical cavity size L^* exists as f approaches 85 Hz, which can be seen in Fig. 11c. This specific frequency coincides with the frequency at which the critical vibra-

tion acceleration, $a^* = 4\pi^2 f^2 A^*$, is largest, see the inset of Fig. 11b. This non-monotonic behavior is likely indicating a change in the physics of the raft around the cavity. For $f < 85$ Hz, the cavity assumes an irregular shape that changes slightly over time, with an example being Fig. 2h for $f = 75$ Hz. In contrast, for $f \geq 85$ Hz, the cavity maintains a circular and stable shape, as in Fig. 11a for $f = 90$ Hz. In particular, Fig. 11a is a time-averaged image, showing that particles immediately surrounding the cavity have large fluctuations in their positions as the time-averaged image is blurry. For particles located approximately ten layers further from the cavity, the corresponding image is not blurry, indicating a strong caging effect. This means that the circular-shaped cavitation occurs against elastic-like resistance from the raft in a glassy state, whereas the irregular-shaped cavity expands under little resistance from the raft in a liquid-like state.

VII. CONCLUSION

Our work demonstrates that particle packing fraction, vibration frequency, and amplitude serve as the primary control parameters for the dynamic behavior of vertically vibrated granular rafts. By systematically tuning these parameters, we map a comprehensive phase diagram spanning from classical Faraday wave patterns to particle dynamics-dominated regimes, including persistent cavities and a dense glassy state. Their occurrence

and transitions are governed by the interplay between the hydrodynamics of vibrated liquid interfaces and the dissipative particle interactions, which at higher packing densities involves elastic-like mechanical response and glassy dynamics.

The vertically vibrated raft experiments establish a new model system for understanding the physics of out-of-equilibrium particle systems, such as the glass transition, the deformation of amorphous solids at finite (effective) temperatures, and the dynamics of poly-crystals if monodisperse particles are used. Different from the commonly considered interaction potentials such as the Lennard-Jones and hard spheres, the interaction potential between particles at vibrated interfaces is complex, with a many-body nature that arises from the capillary and hydrodynamic effects. This interaction can be controlled by manipulating the particle size, density, and the contact angle [10], and additional active particle dynamics can be introduced via manipulating particle shapes [32–34]. Being able to understand how these real-world complexities influence the essential physics of interfacial systems will also have important implications in the creation of dynamically responsive and configurable particle systems.

ACKNOWLEDGMENTS

The authors would like to acknowledge the funding from the National Science Foundation grant CMMI-2519512. We thank Yue Fan, Richard Lueptow, and Paul Umbanhowar for helpful discussions.

-
- [1] S. Protière, Particle rafts and armored droplets, *Annu. Rev. Fluid Mech.* **55**, 459 (2023).
 - [2] M. Nicolson, The interaction between floating particles, *Proc. Cambridge Philos. Soc.* **45**, 288 (1949).
 - [3] P. Kralchevsky and K. Nagayama, Capillary interactions between particles bound to interfaces, liquid films and biomembranes, *Adv. Colloid Interface Sci.* **85**, 145 (2000).
 - [4] D. Vella and L. Mahadevan, The “cheerios effect”, *Am. J. Phys.* **73**, 817 (2005).
 - [5] H. Xiao, R. J. Ivancic, and D. J. Durian, Strain localization and failure of disordered particle rafts with tunable ductility during tensile deformation, *Soft Matter* **16**, 8226 (2020).
 - [6] H. Xiao, G. Zhang, E. Yang, R. Ivancic, S. Ridout, R. Riggelman, D. J. Durian, and A. J. Liu, Identifying microscopic factors that influence ductility in disordered solids, *Proc. Natl. Acad. Sci. U. S. A.* **120**, e2307552120 (2023).
 - [7] G. Hostache and J. H. Mol, Reproductive biology of the neotropical armoured catfish *hoplosternum littorale* (siluriformes—callichthyidae): a synthesis stressing the role of the floating bubble nest, *Aquat. Living Resour.* **11**, 173 (1998).
 - [8] N. J. Mlot, C. A. Tovey, and D. L. Hu, Fire ants self-assemble into waterproof rafts to survive floods, *Proc. Natl. Acad. Sci. U. S. A.* **108**, 7669 (2011).
 - [9] T. H. Tan, A. Mietke, J. Li, Y. Chen, H. Higinbotham, P. J. Foster, S. Gokhale, J. Dunkel, and N. Fakhri, Odd dynamics of living chiral crystals, *Nature* **607**, 287 (2022).
 - [10] M.-J. Dalbe, D. Cosic, M. Berhanu, and A. Kudrolli, Aggregation of frictional particles due to capillary attraction, *Phys. Rev. E* **83**, 051403 (2011).
 - [11] A. Dani, G. Keiser, M. Yeganeh, and C. Maldarelli, Hydrodynamics of particles at an oil-water interface, *Langmuir* **31**, 13290 (2015).
 - [12] B. L. Kim, A. Rendos, P. Ganesh, and K. A. Brown, Failure of particle-laden interfaces studied using the funnel method, *Colloid Interface Sci. Commun.* **28**, 54 (2019).
 - [13] K.-Î. Tô and S. R. Nagel, Rifts in rafts, *Soft Matter* **19**, 905 (2023).
 - [14] D. Vella, P. Aussillous, and L. Mahadevan, Elasticity of an interfacial particle raft, *Europhys. Lett.* **68**, 212 – 218 (2004).
 - [15] C. Peco, W. Chen, Y. Liu, M. M. Bandi, J. E. Dolbow, and E. Fried, Influence of surface tension in the surfactant-driven fracture of closely-packed particulate monolayers, *Soft Matter* **13**, 5832 (2017).
 - [16] Y. Sasaki and H. Katsuragi, Constitutive flow law for hydrogel granular rafts near the brittle-ductile transition (2026), arXiv:2602.08217 [cond-mat.soft].

- [17] R. Aveyard, J. H. Clint, D. Nees, and V. N. Paunov, Compression and structure of monolayers of charged latex particles at air/water and octane/water interfaces, *Langmuir* **16**, 1969 – 1979 (2000).
- [18] R. Aveyard, J. H. Clint, D. Nees, and N. Quirke, Structure and collapse of particle monolayers under lateral pressure at the octane/aqueous surfactant solution interface, *Langmuir* **16**, 8820 (2000).
- [19] D. Vella, H.-Y. Kim, P. Aussillous, and L. Mahadevan, Dynamics of surfactant-driven fracture of particle rafts, *Phys. Rev. Lett.* **96**, 178301 (2006).
- [20] D. Y. Zang, E. Rio, D. Langevin, B. Wei, and B. P. Binks, Viscoelastic properties of silica nanoparticle monolayers at the air-water interface, *Eur. Phys. J. E: Soft Matter Biol. Phys.* **31**, 125 (2010).
- [21] M. Abkarian, S. Protière, J. M. Aristoff, and H. A. Stone, Gravity-induced encapsulation of liquids by destabilization of granular rafts, *Nat. Commun.* **4**, 1895 (2013).
- [22] S. Protière, C. Jossierand, J. M. Aristoff, H. A. Stone, and M. Abkarian, Sinking a granular raft, *Phys. Rev. Lett.* **118**, 108001 (2017).
- [23] B. C. Druecke, R. Mukherjee, X. Cheng, and S. Lee, Collapse of a granular raft: Transition from single particle falling to collective creasing, *Phys. Rev. Fluids* **8**, 024003 (2023).
- [24] M. J. Sayyari and J. B. Bostwick, Destabilizing a buoyant multilayer granular raft by heavy grains: The role of inertia, *Langmuir* **41**, 18403 (2025).
- [25] P. Kralchevsky, I. Ivanov, K. Ananthapadmanabhan, and A. Lips, On the thermodynamics of particle-stabilized emulsions: Curvature effects and catastrophic phase inversion, *Langmuir* **21**, 50 (2005).
- [26] R. Aveyard, J. Clint, and T. Horozov, Aspects of the stabilisation of emulsions by solid particles: Effects of line tension and monolayer curvature energy, *Phys. Chem. Chem. Phys.* **5**, 2398 (2003).
- [27] K. Danov, B. Pouligny, and P. Kralchevsky, Capillary forces between colloidal particles confined in a liquid film: The finite-meniscus problem, *Langmuir* **17**, 6599 (2001).
- [28] C. Planchette, E. Lorenceau, and A.-L. Biance, Surface wave on a particle raft, *Soft Matter* **8**, 2444 (2012).
- [29] L. Saddinger, A. Palotai, M. Aksil, M. Tsamados, and M. Berhanu, Breaking of a floating particle raft by water waves, *Phys. Rev. Fluids* **9**, 094302 (2024).
- [30] H. Pak and R. Behringer, Surface waves in vertically vibrated granular materials, *Phys. Rev. Lett.* **71**, 1832 (1993).
- [31] A. Lagarde and S. Protière, Probing the erosion and cohesion of a granular raft in motion, *Phys. Rev. Fluids* **5**, 044003 (2020).
- [32] J.-W. Barotta, S. J. Thomson, L. F. L. Alventosa, M. Lewis, and D. M. Harris, Bidirectional wave-propelled capillary spinners, *Commun. Phys.* **6**, 87 (2023).
- [33] N. Sungar, J. Sharpe, L. Ijzerman, and J.-W. Barotta, Synchronization and self-assembly of free capillary spinners, *Phys. Rev. E* **111**, 035104 (2025).
- [34] J.-W. Barotta, G. Pucci, E. Silver, A. Hooshanginejad, and D. M. Harris, Synchronization of wave-propelled capillary spinners, *Phys. Rev. E* **111**, 035105 (2025).
- [35] J.-W. Barotta, C. M. Barotta, E. Silver, and D. M. Harris, Macroscopic brownian motion on a chaotic fluid interface (2025), arXiv:2512.15917 [physics.ed-ph].
- [36] M. Faraday, Xvii. on a peculiar class of acoustical figures; and on certain forms assumed by groups of particles upon vibrating elastic surfaces, *Philos. Trans. R. Soc. London* , 299 (1831).
- [37] S. Douady, Experimental study of the faraday instability, *J. Fluid Mech.* **221**, 383 (1990).
- [38] W. S. Edwards and S. Fauve, Patterns and quasi-patterns in the faraday experiment, *J. Fluid Mech.* **278**, 123 (1994).
- [39] W. Batson, F. Zoueshtiagh, and R. Narayanan, The faraday threshold in small cylinders and the sidewall non-ideality, *J. Fluid Mech.* **729**, 496 (2013).
- [40] J. Miles, On faraday waves, *J. Fluid Mech.* **248**, 671 (1993).
- [41] S. Zhang, A. G. L. Borthwick, and Z. Lin, Pattern evolution and modal decomposition of faraday waves in a brimful cylinder, *J. Fluid Mech.* **974**, A56 (2023).
- [42] X. Shao, P. Wilson, J. R. Saylor, and J. B. Bostwick, Surface wave pattern formation in a cylindrical container, *J. Fluid Mech.* **915**, A19 (2021).
- [43] F. Melo, P. Umbanhowar, and H. L. Swinney, Transition to parametric wave patterns in a vertically oscillated granular layer, *Phys. Rev. Lett.* **72**, 172 (1994).
- [44] P. B. Umbanhowar, F. Melo, and H. L. Swinney, Localized excitations in a vertically vibrated granular layer, *Nature* **382**, 793 (1996).
- [45] F. Rouyer and N. Menon, Velocity fluctuations in a homogeneous 2d granular gas in steady state, *Phys. Rev. Lett.* **85**, 3676 (2000).
- [46] K. Feitosa and N. Menon, Breakdown of energy equipartition in a 2d binary vibrated granular gas, *Phys. Rev. Lett.* **88**, 198301 (2002).
- [47] J. Deseigne, O. Dauchot, and H. Chaté, Collective motion of vibrated polar disks, *Physical review letters* **105**, 098001 (2010).
- [48] C. Scholz, M. Engel, and T. Pöschel, Rotating robots move collectively and self-organize, *Nat. Comm.* **9**, 931 (2018).
- [49] Z. Zheng, C. Jiang, Y. Chen, M. Baggioli, and J. Zhang, Topological signatures of collective dynamics and turbulent-like energy cascades in apolar active granular matter, *Proc. Nat. Acad. Sci. U. S. A.* **123**, e2510873123 (2026).
- [50] K. Kumar and L. S. Tuckerman, Parametric instability of the interface between two fluids, *J. Fluid Mech.* **279**, 49 (1994).
- [51] T. B. Benjamin and F. Ursell, The stability of the plane free surface of a liquid in vertical periodic motion, *Proc. R. Soc. A* **225**, 505 (1954).
- [52] T. Atherton and D. Kerbyson, Size invariant circle detection, *Image and Vision Computing* **17**, 795 (1999).
- [53] M. Ghadiri and R. Krechetnikov, Controlling chaos by the system size, *Sci. Rep.* **11**, 8703 (2021).
- [54] E. Xueauan and G. Yuxin, Ordered and chaotic modes of surface wave patterns in a vertically oscillating fluid, *Commun. Nonlinear Sci. Numer. Simul.* **1**, 1 (1996).
- [55] L. D. Landau, L. Pitaevskii, A. M. Kosevich, and E. M. Lifshitz, *Theory of elasticity: volume 7*, Vol. 7 (Elsevier, 2012).
- [56] P. Aussillous and D. Quéré, Properties of liquid marbles, *Proc. R. Soc. London A* **462**, 973 (2006).
- [57] P. G. Debenedetti and F. H. Stillinger, Supercooled liquids and the glass transition, *Nature* **410**, 259 (2001).
- [58] M. D. Ediger, Spatially heterogeneous dynamics in supercooled liquids, *Annu. Rev. Phys. Chem.* **51**, 99 (2000).
- [59] O. Dauchot, G. Marty, and G. Biroli, Dynamical het-

- erogeneity close to the jamming transition in a sheared granular material, *Phys. Rev. Lett.* **95**, 265701 (2005).
- [60] A. Mehta, Spatial, dynamical and spatiotemporal heterogeneities in granular media, *Soft Matter* **6**, 2875 (2010).
- [61] A. S. Keys, A. R. Abate, S. C. Glotzer, and D. J. Durian, Measurement of growing dynamical length scales and prediction of the jamming transition in a granular material, *Nat. Phys.* **3**, 260 (2007).